Microfossils with tail-like structures in the 3.4 Gyr old Strelley Pool Formation Authors

Frédéric Delarue, Sylvain Bernard, Kenichiro Sugitani, François Robert, Romain Tartèse, Sonja-Verena Albers, Rémi Duhamel, Sylvain Pont, Sylvie Derenne

Microfossils with tail-like structures in the 3.4 Gyr old Strelley Pool Formation

Authors

Frédéric Delarue[a]*, Sylvain Bernard[b], Kenichiro Sugitani[c], François Robert[b], Romain Tartèse[d], Sonja-Verena Albers[e,f], Rémi Duhamel[b], Sylvain Pont[b], Sylvie Derenne[a]

Affiliations

[a]Sorbonne Université, CNRS, EPHE, PSL, UMR 7619 METIS, 4 place Jussieu, F-75005 Paris, France

[b]Muséum National d'Histoire Naturelle, Sorbonne Université, UMR CNRS 7590, IRD, Institut de Minéralogie, de Physique des Matériaux et de Cosmochimie, IMPMC, 75005 Paris, France

[c]Department of Earth and Environmental Sciences, Graduate School of Environmental Studies, Nagoya University, Nagoya, Japan

[d]Department of Earth and Environmental Sciences, The University of Manchester, Manchester M13 9PL, United Kingdom

[e]Molecular Biology of Archaea, Institute of Biology II, Faculty of Biology, University of Freiburg, Freiburg, Germany.

[f]Spemann Graduate School of Biology and Medicine, University of Freiburg, Freiburg, Germany.

*Correspondence to: frederic.delarue@upmc.fr

Abstract

Some of the oldest traces for planktonic lifestyle have been reported in ca. 3.4 billion years old silicified sediments from the Strelley Pool Formation in Western Australia. Observation of flange appendages suggests that Archean life motility was passive and driven by drifting of microorganisms in their surrounding environment. Until now, the oldest traces for active motility are ca. 2.1 billion years old. Whether or not active motility already existed during the Archean eon remains an open question. In this study, we report the discovery of new 3.4 billion years old microfossils exhibiting a tail-like structure isolated from the Strelley Pool Formation. Exhibiting Raman spectra typically observed in organic-walled microfossils from the Strelley Pool Formation, these microfossils exhibiting a tail-like structure are syngenetic with their host rock. Composed of carbon, nitrogen, and, for one specimen, phosphorus, some of these organic-walled microfossils also exhibit significant level of aliphatic and amide moieties supporting their biogenicity. In addition, these microfossils exhibit a tail-like appendage sharing similar morphological features with locomotory organelles in modern microorganisms such as archaella, flagella, and cilia. This suggests that this observed appendage likely provided them with movement capabilities. If correct, with the ability to move, these microorganisms were capable of escaping from harsh environments and/or colonizing new ecological niches as early as 3.4 billion years ago.

Keywords

Archean – Early life - Morphology - NanoSIMS - Raman spectroscopy - Strelley Pool

1. Introduction

Archean carbonaceous microfossils testify for the widespread presence of life on Earth as early as ca. 3.4 billion years ago (Westall et al., 2006; Sugitani et al., 2010; Wacey et al., 2011; Alleon et al., 2018). However, the interpretation of the Archean palaeobiological record is fraught with

52 difficulties pertaining to fossilization and burial-induced degradation processes, as exemplified
53 by intense debates over the past couple of decades (e.g., Schopf et al., 2002; Brasier et al., 2002;
54 Wacey et al., 2016). Remnants of early life forms have experienced burial and thermal alteration
55 for billions of years, which led to the degradation of many pristine biological traits (Javaux et
56 al., 2019). Archean putative microfossils tend to exhibit simple morphological shapes at the
57 micrometric scale (e.g., spheroidal, filamentous, film, and lenticular forms) that can also be
58 abiotically produced (Garcia-Ruiz et al., 2003; Cosmidis et al., 2016), precluding, in turn, any
59 simple morphological distinction between genuine biological remnants and mineral/organic
60 biomorphs. Because of the lack of taxonomically informative features (Javaux et al., 2019),
61 morphological criteria alone are generally considered as insufficient to assess the biological
62 nature of ancient traces of life in the Archean geological record (Brasier et al., 2006). As a
63 result, the ancient fossil record has not yet conveyed a complete picture of ancient biodiversity.
64 Here, we report the discovery of 3.4 billion years old organic microfossils from the Strelley
65 Pool Formation (SPF) exhibiting exceptionally preserved morphological traits possibly
66 indicative of active motility.
67
68

2. Material and methods

2.1. Studied sample

For this study, we selected a 3.4 billion year-old black chert sampled from the Panorama locality (PANX1-1) situated in the SPF (Western Australia), and which displays abundant microfossils and microscopically identifiable parallel laminations (see Sugitani et al., 2010, 2013, and 2015 for detailed description of the geological background).

2.2. Chemical isolation of microfossils

Organic-walled microfossils were isolated from the SPF carbonaceous black chert sample using a modified version of the classical acid maceration procedure (Delarue et al., 2020). A 'soft' acid maceration procedure was applied in order to minimize both potential physical and chemical degradation of organic microstructures. Prior to acid maceration, about 30 g of rock samples were fragmented into ~3 g rock chips rather than crushed into finer grains. Rock chips were cleaned using ultrapure water and a mixture of dichloromethane/methanol (v/v: 2/1), and were then directly placed in a Teflon vessel filled with a mixture of HF (40%, reagent grade) / HCl (37%; reagent grade; v/v: 9/1) at room temperature. After 48 hours, successive centrifugation and rinsing steps using ultrapure water were performed until reaching neutrality. The residual material was suspended in ethanol and filtered on polycarbonate filters (pore Ø = 10 µm). After ethanol evaporation, polycarbonate filters were fixed on carbon tape and coated with 20 nm of gold to prevent further contamination by atmospheric deposits and for further analyses.

2.3. Scanning electron microscopy and Energy Dispersive X-Ray Spectroscopy (SEM-EDXS)

SEM-EDXS imaging and analysis were performed on gold-coated filters using a TESCAN VEGA II at the French National Museum of Natural History (MNHN) operated with an accelerating voltage of 15 kV.

2.4. Raman spectroscopy

Raman microspectroscopy was carried out using a Renishaw InVIA microspectrometer equipped with a 532 nm green laser. The laser was focused on the sample by using a DMLM Leica microscope with a 50× objective. The spectrometer was first calibrated with a silicon standard before the analytical session (matching at 520.5 cm^{-1}). For each target, we determined the Raman shift intensity in the 1000 to 2000 cm^{-1} spectral window that includes the first-order defect (D) and graphite (G) peaks. A laser power below 1 mW was used to prevent any thermal alteration during spectrum acquisition. Spectrum acquisition was achieved after three iterations using a time exposure of 10 seconds (spectral resolution of 1.5 cm^{-1}). Raman microspectroscopy was performed on gold-coated organic surfaces, implying a slight lowering of the relative intensity of the D band with respect to the G one (Delarue et al. 2020).

2.5. Nanoscale secondary ion mass spectrometry

Isolated microfossils were analyzed using a CAMECA NanoSIMS 50 ion probe using a Cs^+ primary ion beam. Before measurements, pre-analysis sputtering was performed over 30 × 30 μm^2 areas for ca. 8 minutes using a 500 pA primary current (750 µm aperture diaphragm) to remove surficial contamination, and achieve Cs^+ saturation fluence and constant secondary ion count rates. Analyses were then carried out using a 10 pA primary current (200 µm aperture diaphragm) on smaller areas to avoid pre-analysis sputtering edge artifacts. The secondary molecular species $^{12}C^{14}N^-$ and $^{31}P^-$ were collected simultaneously in electron multipliers. The

NanoSIMS raw data were corrected for a 44 ns dead time on each electron multiplier and processed using the Limage software.

2.6. Focused ion beam (FIB)

FIB ultrathin sections were extracted from the organic microfossils using an FEI Strata DB 235 (IEMN, Lille, France). Milling at low gallium ion currents minimizes common artefacts, including local gallium implantation, mixing of components, creation of vacancies or interstitials, creation of amorphous layers, redeposition of the sputtered material on the sample surface, and significant changes in the speciation of carbon-based polymers.

2.7. Scanning transmission X-ray microscopy (STXM)

X-ray Absorption Near Edge Structure (XANES) investigations were conducted using the HERMES STXM beamline at the synchrotron SOLEIL (Gif-sur-Yvette, France). Carbon contamination on beamline optics was constantly removed thanks to a continuous flow of pure O_2. The well-resolved 3p Rydberg peak of gaseous CO_2 at 294.96 eV was used for energy calibration. Collecting image stacks at energy increments of 0.1 eV with a dwell time of $\leq$ 1 ms per pixel prevented irradiation damage. The estimations of N/C values and the normalization of the C-XANES spectra shown here were done using QUANTORXS (Le Guillou et al., 2018).

3. Results and Discussion

Microscope observations of the studied SPF sample thin sections revealed the presence of organic-walled microfossils exhibiting a tail-like structure (Fig. 1a, b). These microfossils are exclusively observed within the siliceous sedimentary matrix, precluding their introduction during hydrothermal fluid circulation post 3.4 Ga.

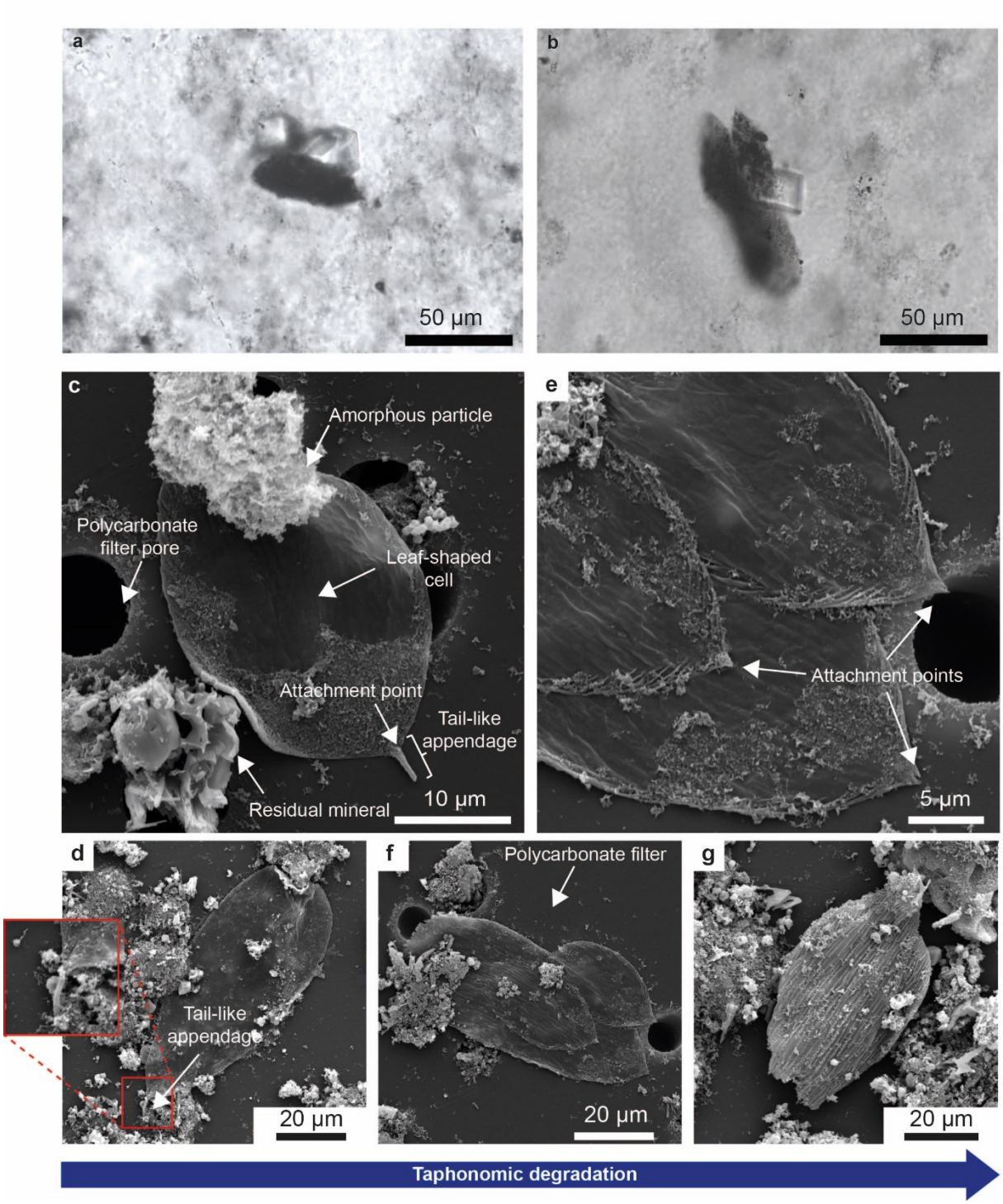

141

142 **Figure 1: Thin section micrographs and scanning electron microscopy images of organic**
143 **microfossils** exhibiting or not a tail-like structure**.** (a) Micrograph presenting a microfossil
144 exhibiting a tail-like structure embedded in the main siliceous matrix of the studied SPF chert.
145 (b) Micrograph presenting a microfossil exhibiting no tail-like structure. (c-f) SEM images of
146 organic microfossils exhibiting or not a tail-like structure isolated by acid maceration. (c,d)
147 Exceptionally-well preserved leaf-shaped cells presenting a locomotory organelle composed of
148 an attachment point and of a tail; (e-g) Corresponding degraded organic-walled microfossils
149 lacking a tail but (e, f) exhibiting an attachment point. Comparison between microfossils

exhibiting a tail-like structure and microfossils presenting an attachment point suggests that tails may be lost during taphonomy. A taphonomic degradation gradient is observed from the left to the right. Classic taphonomical degradation features, including folds and tears, are observed.

Raman spectra of specimens exhibiting a tail-like structure chemically isolated from the siliceous matrix are typical of those of disordered carbonaceous materials having undergone a low-grade metamorphism (Fig. 2a; Pasteris and Wopenka, 2003). Their Raman line shapes suggest that these microfossils experienced hydrothermal and/or diagenetic peak temperatures of approximately 250-300 °C (Lahfid et al., 2010; Kouketsu et al., 2014). Raman first-order spectra of the studied SPF microfossils exhibiting a tail-like structure are similar to those previously determined on syngenetic microfossils from the same geological formation observed in thin sections (Lepot et al., 2013; Sugitani et al., 2013), on freshly fractured faces (Alleon et al., 2018), and in acid maceration residue (Delarue et al., 2020). Therefore, these organic-walled microfossils exhibiting a tail-like structure should be regarded as syngenetic as they were subjected to the maximum metamorphic temperature registered by their host rock.

Although Raman spectroscopy is a useful tool to assess syngeneity, it is not sufficient to determine the biogenicity of putative remains of ancient life (Pasteris and Wopenka, 2003). Energy-dispersive X-ray spectroscopy data show that the studied specimens essentially contain C and O (Fig. 2b), confirming their organic nature, while nanoscale secondary ion mass spectrometry reveals the presence of nitrogen and, in one specimen, phosphorus (Figs. 2d, f-g). The presence of these key elements of cell walls, proteins, and nucleic acids are consistent with a biological origin.

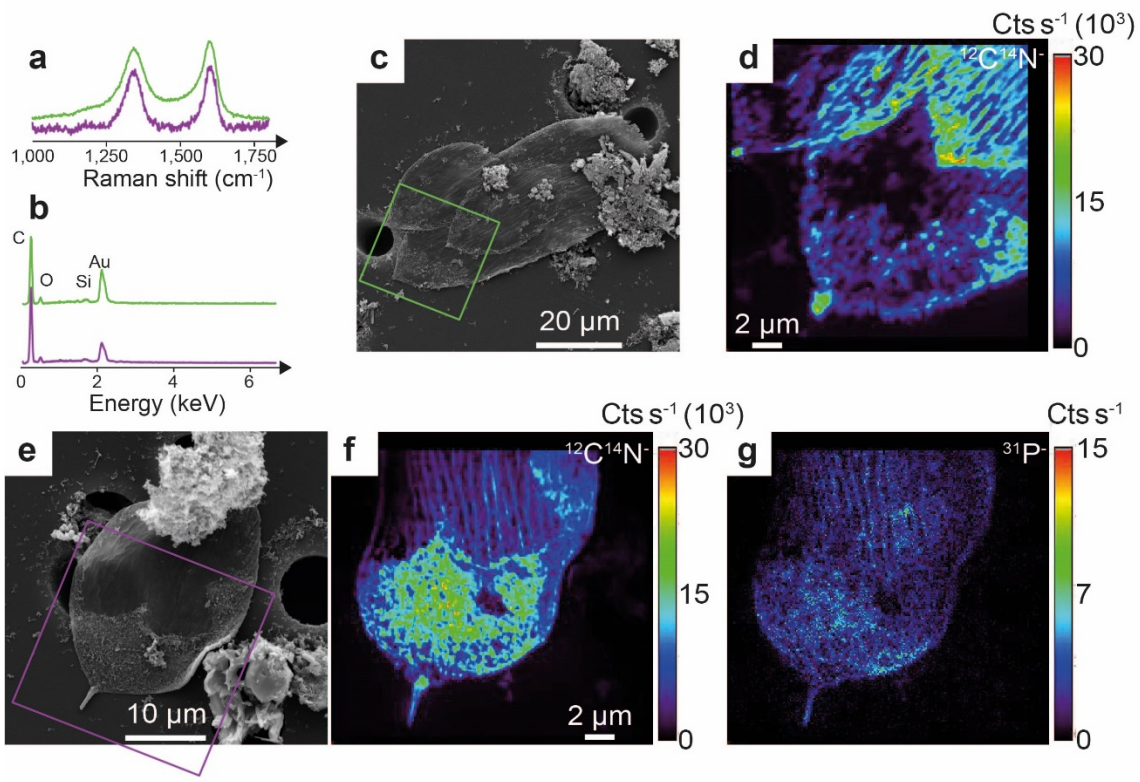

Figure 2: Raman spectra, energy-dispersive X-ray spectra, and nanoscale secondary ion mass spectrometry images. (a) First-order Raman spectra determined on isolated organic microfossils exhibiting a tail-like structure and (b) corresponding energy-dispersive X-ray spectra. Green and purple lines indicate that spectra were acquired on specimens shown in panels c and e, respectively. (c, e) SEM images of organic-walled microfossils investigated by EDXS, Raman spectroscopy and NanoSIMS. Green and purple squares indicate areas probed by NanoSIMS. (d, f) The $^{12}C^{14}N^-$ ion images illustrate the presence of nitrogen. (g) The $^{31}P^-$ image illustrates the presence of phosphorus. No $^{31}P^-$ was recorded on the second specimen shown in panel c. Variations in $^{31}P^-$ emission intensity between the smooth (e.g., microfossil itself) and rough (e.g., coating by amorphous submicrometric organic matter) surfaces cannot be used to depict any P enrichment because of microtopographic features biasing ion emissions (Delarue et al., 2017).

Spatially resolved chemical investigations exploiting X-ray absorption confirm the heterogeneous chemical nature of the investigated organic-walled microfossils: at least three different types of chemical structures could be distinguished within a given specimen (Fig. 3). Specimens contain some highly graphitic organic materials with almost no nitrogen as revealed by X-ray absorption spectra exhibiting a broad peak of conjugated aromatic groups (285.5 eV) and the excitonic absorption feature of planar domains of highly conjugated π systems (291.7

eV; Bernard et al., 2010). Closely associated are N-poor materials with XANES spectra similar to those of thermally-altered kerogen with an intense absorption peak at 285 eV (aromatic or olefinic groups), a relatively broad absorption feature at 287.5 eV (aliphatic carbons), and an absorption feature at 286.6 eV (imine, nitrile, carbonyl and/or phenol groups; Bernard et al., 2010; Le Guillou et al., 2018). Specimens also contain N-rich compounds (N/C ~ 0.22) with XANES spectra that exhibit clear contributions of quinones or cyclic amides (284.5 eV), aromatic or olefinic carbons (285.1 eV), imine, nitrile, carbonyl and/or phenol groups (286.6 eV), aliphatics (287.7 eV) and amides (288.2 eV**)**. Altogether, the chemical structure of the SPF specimen investigated here is consistent with the preservation of partially degraded biomolecules.

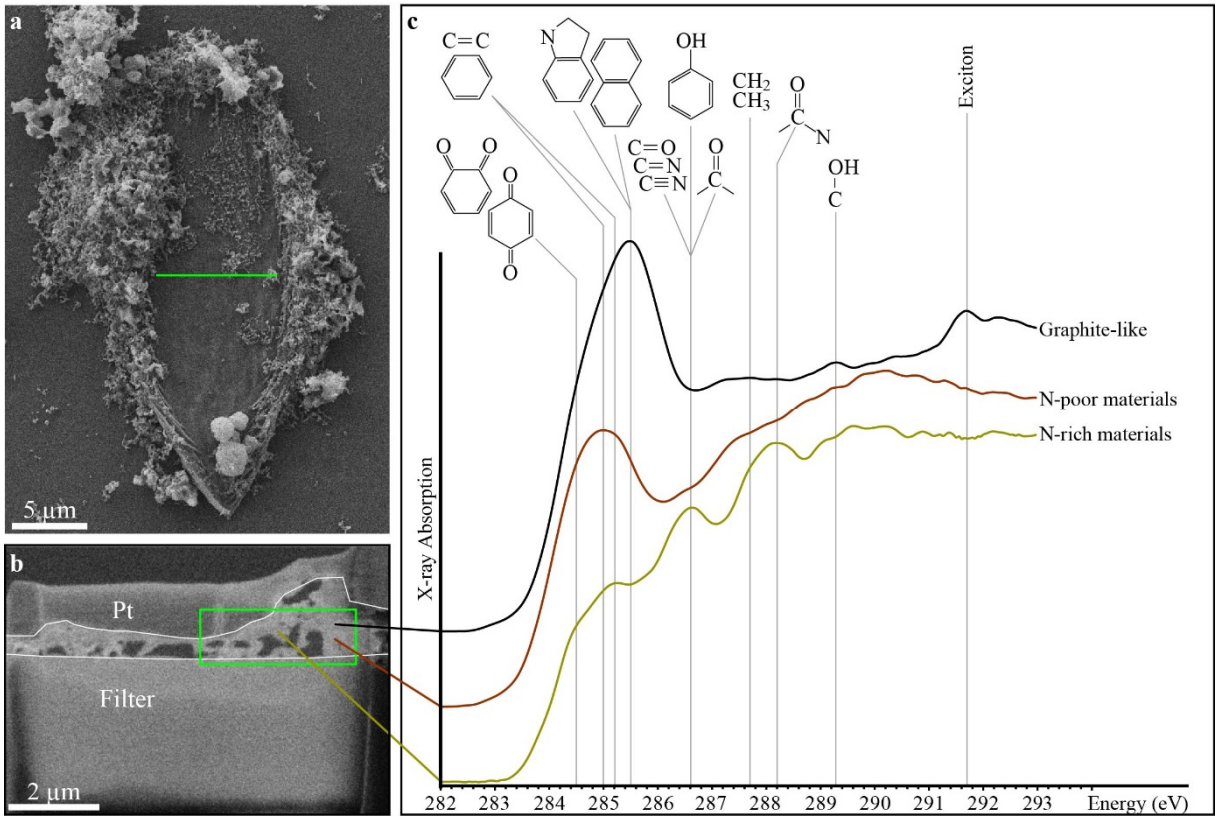

Figure 3: Scanning transmission X-ray microscopy-based X-ray absorption near edge structure characterization. (a) SEM image of the specimen from which a focused ion beam foil has been extracted (green line). (b) SEM image of the focused ion beam foil evidencing the limited thickness of the specimen. The green square indicates the area investigated using

STXM. (c) Carbon-X-ray absorption near edge structure spectra of the organic materials composing the investigated specimen.

From a morphological point of view, the organic-walled microfossils are leaf-shaped cells ranging from 30 to 84 µm in length and from 16 to 37 µm in width (Fig. 1). They exhibit classic taphonomical degradation features, including folds and tears (Figs. 1c-g). The preparation of ultrathin foils using focused ion beam illustrates their relative limited thickness, ranging from 200 to 500 nm (Fig. 3). Four specimens also exhibit a specific morphological feature: a tail-like appendage protruding from the leaf-shaped cell (Figs. 1c, d).

From the comparison with modern microorganisms, we can assume that this tail-like appendage is a remnant of an ancient prostheca or of a locomotory organelle. The tail-like appendages observed in SPF microfossils are between 0.7 and 1.2 µm in diameter, which is, by far, larger than those reported for modern archaella, flagella, and cilia, reaching ca. 10, 20, and 200 nm, respectively (Jarell and McBride, 2008; Beeby et al., 2020). This would be forgetting that Precambrian organic-walled microfossils exhibit very large cell dimensions (Ø > 10 µm) compared to modern microorganisms (Javaux et al., 2010; Sugitani et al., 2010; 2015; Balidukay et al., 2016; Loron et al., 2019.

In order to take this difference into account, we propose to use the Appendage Shape Index (ASI), which is based on the ratio between the width of the tail-like appendage and that of the parent cell (Fig. 4). Compilation of morphometric data from extant microorganisms shows that prosthecae and locomotory organelles are characterized by different ASI values. Prosthecae display ASI values ranging from 13 to 39 % while they range from 1 to 10 % for modern archaella, flagella, and cilia (Fig. 4; see supplementary information for detailed values). In the

present study, the tail-like appendages are characterized by ASI values ranging from 2 to 6 %, that is values falling within the domain of modern archaella, flagella, and cilia (Fig. 4).

Involved in anchoring cells to organic and mineral surfaces, in nutrient uptake, or in asexual reproduction by budding at its tip (Curtis, 2017), a prostheca is a micrometric tube-like appendage consisting in an extension of the cellular membrane. This implies a structural continuity between the microorganism body and the base of the prostheca (Javaux *et al*., 2003). Here, the SPF specimens investigated exhibit an anchoring attachment point and a filament-like appendage, indicating two distinct structural subunits (Fig. 1) at odds with any extension of the cellular membrane. Because of their ASI values and their two structural subunits, the tail-like appendages observed in SPF microfossils cannot be considered as remnants of prosthecae.

As far as we are aware, occurrence of distinct external and functional subunits can only be assigned to locomotory organelles, in good agreement with ASI values. However, these subunits do not meet standard structural features (for instance, a curved hook connecting the filament to the basal body in flagella) observed on locomotory organelles from any organism of the three extant domains of life (see Khan and Scholey, 2018) implying in turn, that the observed structural features do not allow to depict the biological affinity of these remnants of tailed microorganisms..

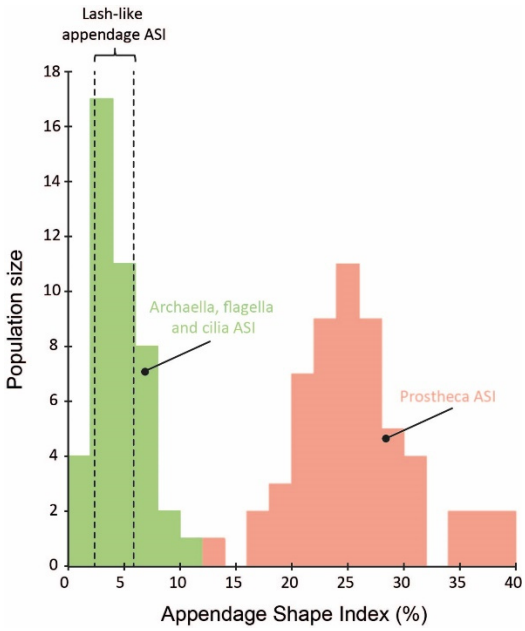

Figure 4: Compilation of Appendage Shape Indices determined on extant microorganisms and on studied microfossils. ASI was computed according to the ratio between the width of appendage (archaellum, flagellum, cilium and prostheca) and that of its parent cell (×100). Each width of appendage and of its parent cell was determined graphically based on micrographs and images published in Southam et al. (1990), Poindexter and Staley (1996), Furuno et al. (1997), Wustman et al. (1997), Quintero et al. (1998), Wang et al. (2000), Miller et al. (2004), Bergholtz et al. (2006), Vasilyeva et al. (2006), Wagner et al. (2006), Kanbe et al. (2007), Abraham et al. (2008), Nge et al. (2008), Pyatibratov et al. (2008), Siano et al. (2009), Craveiro et al. (2010), Wang et al. (2011), Abraham and Rohde (2014), Lim et al. (2014), Albers and Jarrell (2015), Deng et al. (2016), Kinosita and Nishizaka (2016), Sugitomo et al. (2016), Curtis (2017), and Leander et al. (2017; (see supplementary information)). ASI determined on archaella, flagella, and cilia are indicated in green while those determined on prosthecae are indicated in pink. The area delimited by dotted lines indicate ASI determined on four tail-like appendages observed on SPF organic-walled microfossils. ASI ranges from 4.8 to 5.8 % and from 2.2 to 3.3 % in organic-walled microfossil observed in thin sections (n = 2) and in the acid maceration residue (n = 2), respectively. ASI is likely overestimated in thin sections as a consequence of shadows occurring at the edge of microfossils.

Previous reports of 3.4-3.0 Ga lenticular microfossils exhibiting a flange were interpreted as demonstrating passive motility of microbial planktons drifting depending on their surrounding environment (House et al., 2013; Sugitani et al., 2015; Oehler et al., 2017; Kozawa et al., 2019). To date, the oldest evidence for active motility was recorded as tubular sedimentary structures in 2.1 Ga Francevillian sedimentary series in Gabon (El Albani et al., 2019). The preservation of tail-like structures by some SPF microfossils suggests that some microorganisms could have

been capable of active motility – a mechanism whereby microorganisms can direct their movement – as early as 3.4 Gyr ago. Since it likely provided them with the ability to move in the water column or at the surface of organic and/or mineral surfaces, this finding suggests that microorganisms were possibly able to escape harsh environments, adapt their feeding strategies moving towards more favorable nutrient sources, and colonize new ecological niches less than a billion years after the Earth became habitable.

Acknowledgments

We thank D. Troadec (IEMN) for FIB extraction. We also acknowledge The National NanoSIMS Facility at the MNHN, supported by MNHN, CNRS, Région Ile de France, and Ministère de l'Enseignement Supérieur et de la Recherche. Special thanks go to Stefan Stanescu and Sufal Swaraj for their expert support with the HERMES STXM beamline at SOLEIL. The HERMES beamline (SOLEIL) is supported by the CNRS, the CEA, the Region Ile de France, the Departmental Council of Essonne and the Region Centre. This work was supported by the Programme National de Planétologie (PNP) of CNRS/INSU, co-funded by CNES R.T. also acknowledges the UK Science and Technology Facilities Council (grant ST/P005225/1) for financial support. Authors are grateful to the associate editor and the two anonymous reviewers for their constructive comments.

References

Abraham, W.-R., Macedo, A.J., Lunsdorf, H., Fischer, R., Pawelczyk, S., Smit, J., Vancanneyt, M., 2008. Phylogeny by a polyphasic approach of the order Caulobacterales, proposal of Caulobacter mirabilis sp. nov., Phenylobacterium haematophilum sp. nov. and

304 Phenylobacterium conjunctum sp. nov., and emendation of the genus Phenylobacterium.
305 International Journal of Systematic and Evolutionary Microbiology 58, 1939–1949.
306 Abraham, W.-R., Rohde, M., 2014. The Family Hyphomonadaceae, in: Rosenberg, E., DeLong,
307 E.F., Lory, S., Stackebrandt, E., Thompson, F. (Eds.), The Prokaryotes. Springer Berlin
308 Heidelberg, Berlin, Heidelberg, pp. 283–299.
309 Albers, S.-V., Jarrell, K.F., 2015. The archaellum: how archaea swim. Frontiers in
310 Microbiology 6. doi:10.3389/fmicb.2015.00023
311 Alleon, J., Bernard, S., Le Guillou, C., Beyssac, O., Sugitani, K., Robert, F., 2018. Chemical
312 nature of the 3.4 Ga Strelley Pool microfossils. Geochemical Perspectives Letters 37–42.
313 Baludikay, B.K., Storme, J.-Y., François, C., Baudet, D., Javaux, E.J., 2016. A diverse and
314 exquisitely preserved organic-walled microfossil assemblage from the Meso–Neoproterozoic
315 Mbuji-Mayi Supergroup (Democratic Republic of Congo) and implications for Proterozoic
316 biostratigraphy. Precambrian Research 281, 166–184.
317 Beeby, M., Ferreira, J.L., Tripp, P., Albers, S.-V., Mitchell, D.R., 2020. Propulsive
318 nanomachines: the convergent evolution of archaella, flagella, and cilia. FEMS Microbiology
319 Reviews fuaa006.
320 Bergholtz, T., Daugbjerg, N., Moestrup, O., Fernandez-Tejedor, M., 2006. On the identity of
321 karlodinium veneficum and description of karlodinium armiger sp. nov. (dinophyceae), based
322 on light and electron microscopy, nuclear-encoded lsu rdna, and pigment composition. Journal
323 of Phycology 42, 170–193.
324 Bernard, S., Beyssac, O., Benzerara, K., Findling, N., Tzvetkov, G., Brown, G.E., 2010.
325 XANES, Raman and XRD study of anthracene-based cokes and saccharose-based chars
326 submitted to high-temperature pyrolysis. Carbon 48, 2506–2516.

Brasier, M., McLoughlin, N., Green, O., Wacey, D., 2006. A fresh look at the fossil evidence for early Archaean cellular life. Philosophical Transactions of the Royal Society B: Biological Sciences 361, 887–902.

Brasier, M.D., Green, O.R., Jephcoat, A.P., Kleppe, A.K., Van Kranendonk, M.J., Lindsay, J.F., Steele, A., Grassineau, N.V., 2002. Questioning the evidence for Earth's oldest fossils. Nature 416, 76–81.

Cosmidis, J., Templeton, A.S., 2016. Self-assembly of biomorphic carbon/sulfur microstructures in sulfidic environments. Nature Communications 7, 12812.

Craveiro, S.C., Moestrup, Ø., Daugbjerg, N., Calado, A.J., 2010. Ultrastructure and Large Subunit rDNA-Based Phylogeny of Sphaerodinium cracoviense, an Unusual Freshwater Dinoflagellate with a Novel Type of Eyespot: Sphaerodinium ultrastructure and phylogeny. Journal of Eukaryotic Microbiology 57, 568–585.

Curtis, P.D., 2017. Stalk formation of Brevundimonas and how it compares to Caulobacter crescentus. PLOS ONE 12, e0184063.

Delarue, F., Robert, F., Derenne, S., Tartèse, R., Jauvion, C., Bernard, S., Pont, S., Gonzalez-Cano, A., Duhamel, R., Sugitani, K., 2020. Out of rock: A new look at the morphological and geochemical preservation of microfossils from the 3.46 Gyr-old Strelley Pool Formation. Precambrian Research 336, 105472.

Delarue, F., Robert, F., Sugitani, K., Tartèse, R., Duhamel, R., Derenne, S., 2017. Investigation of the Geochemical Preservation of ca. 3.0 Ga Permineralized and Encapsulated Microfossils by Nanoscale Secondary Ion Mass Spectrometry. Astrobiology 17, 1192–1202.

Deng, Y., Chen, C., Zhao, Z., Zhao, J., Jacq, A., Huang, X., Yang, Y., 2016. The RNA Chaperone Hfq Is Involved in Colony Morphology, Nutrient Utilization and Oxidative and Envelope Stress Response in Vibrio alginolyticus. PLOS ONE 11, e0163689.

El Albani, A., Mangano, M.G., Buatois, L.A., Bengtson, S., Riboulleau, A., Bekker, A., Konhauser, K., Lyons, T., Rollion-Bard, C., Bankole, O., Lekele Baghekema, S.G., Meunier, A., Trentesaux, A., Mazurier, A., Aubineau, J., Laforest, C., Fontaine, C., Recourt, P., Chi Fru, E., Macchiarelli, R., Reynaud, J.Y., Gauthier-Lafaye, F., Canfield, D.E., 2019. Organism motility in an oxygenated shallow-marine environment 2.1 billion years ago. Proceedings of the National Academy of Sciences 116, 3431–3436.

Furuno, M., Atsumi, T., Yamada, T., Kojima, S., Nishioka, N., Kawagishi, I., Homma, M., 1997. Characterization of polar-flagellar-length mutants in Vibrio alginolyticus. Microbiology 143, 1615–1621.

Garcia-Ruiz, J.M., 2003. Self-Assembled Silica-Carbonate Structures and Detection of Ancient Microfossils. Science 302, 1194–1197.

House, C.H., Oehler, D.Z., Sugitani, K., Mimura, K., 2013. Carbon isotopic analyses of ca. 3.0 Ga microstructures imply planktonic autotrophs inhabited Earth's early oceans. Geology 41, 651–654.

Jarrell, K.F., McBride, M.J., 2008. The surprisingly diverse ways that prokaryotes move. Nature Reviews Microbiology 6, 466–476.

Javaux, E.J., 2003. Recognizing and interpreting the fossils of early eukaryotes. Origins of Life and Evolution of the Biosphere 33, 75–94.

Javaux, E.J., 2019. Challenges in evidencing the earliest traces of life. Nature 572, 451–460.

Javaux, E.J., Marshall, C.P., Bekker, A., 2010. Organic-walled microfossils in 3.2-billion-year-old shallow-marine siliciclastic deposits. Nature 463, 934–938.

Kanbe, M., Yagasaki, J., Zehner, S., Göttfert, M., Aizawa, S.-I., 2007. Characterization of Two Sets of Subpolar Flagella in Bradyrhizobium japonicum. Journal of Bacteriology 189, 1083–1089.

375 Khan, S., Scholey, J.M., 2018. Assembly, Functions and Evolution of Archaella, Flagella and
376 Cilia. Current Biology 28, R278–R292.
377 Kinosita, Y., Uchida, N., Nakane, D., Nishizaka, T., 2016. Direct observation of rotation and
378 steps of the archaellum in the swimming halophilic archaeon Halobacterium salinarum. Nature
379 Microbiology 1, 16148.
380 Kouketsu, Y., Mizukami, T., Mori, H., Endo, S., Aoya, M., Hara, H., Nakamura, D., Wallis, S.,
381 2014. A new approach to develop the Raman carbonaceous material geothermometer for low-
382 grade metamorphism using peak width. Island Arc 23, 33–50.
383 Kozawa, T., Sugitani, K., Oehler, D.Z., House, C.H., Saito, I., Watanabe, T., Gotoh, T., 2019.
384 Early Archean planktonic mode of life: Implications from fluid dynamics of lenticular
385 microfossils. Geobiology 17, 113–126.
386 Lahfid, A., Beyssac, O., Deville, E., Negro, F., Chopin, C., Goffé, B., 2010. Evolution of the
387 Raman spectrum of carbonaceous material in low-grade metasediments of the Glarus Alps
388 (Switzerland): RSCM in low-grade metasediments. Terra Nova 22, 354–360.
389 Le Guillou, C., Bernard, S., De la Pena, F., Le Brech, Y., 2018. XANES-Based Quantification
390 of Carbon Functional Group Concentrations. Analytical Chemistry 90, 8379–8386.
391 Leander, B.S., Lax, G., Karnkowska, A., Simpson, A.G.B., 2017. Euglenida, in: Archibald,
392 J.M., Simpson, A.G.B., Slamovits, C.H. (Eds.), Handbook of the Protists. Springer International
393 Publishing, Cham, pp. 1047–1088.
394 Lepot, K., Williford, K.H., Ushikubo, T., Sugitani, K., Mimura, K., Spicuzza, M.J., Valley,
395 J.W., 2013. Texture-specific isotopic compositions in 3.4Gyr old organic matter support
396 selective preservation in cell-like structures. Geochimica et Cosmochimica Acta 112, 66–86.
397 Lim, H.C., Leaw, C.P., Tan, T.H., Kon, N.F., Yek, L.H., Hii, K.S., Teng, S.T., Razali, R.M.,
398 Usup, G., Iwataki, M., Lim, P.T., 2014. A bloom of Karlodinium australe (Gymnodiniales,

399 Dinophyceae) associated with mass mortality of cage-cultured fishes in West Johor Strait,
400 Malaysia. Harmful Algae 40, 51–62.
401 Loron, C.C., Rainbird, R.H., Turner, E.C., Greenman, J.W., Javaux, E.J., 2019. Organic-walled
402 microfossils from the late Mesoproterozoic to early Neoproterozoic lower Shaler Supergroup
403 (Arctic Canada): Diversity and biostratigraphic significance. Precambrian Research 321, 349–
404 374.
405 Miller, T.R., Hnilicka, K., Dziedzic, A., Desplats, P., Belas, R., 2004. Chemotaxis of
406 Silicibacter sp. Strain TM1040 toward Dinoflagellate Products. Applied and Environmental
407 Microbiology 70, 4692–4701.
408 Ng, S.Y.M., Zolghadr, B., Driessen, A.J.M., Albers, S.-V., Jarrell, K.F., 2008. Cell Surface
409 Structures of Archaea. Journal of Bacteriology 190, 6039–6047.
410 Oehler, D.Z., Walsh, M.M., Sugitani, K., Liu, M.-C., House, C.H., 2017. Large and robust
411 lenticular microorganisms on the young Earth. Precambrian Research 296, 112–119.
412 Pasteris, J.D., Wopenka, B., 2003. Necessary, but Not Sufficient: Raman Identification of
413 Disordered Carbon as a Signature of Ancient Life. Astrobiology 3, 727–738.
414 Poindexter, J.S., Staley, J.T., 1996. Caulobacter and Asticcacaulis stalk bands as indicators of
415 stalk age. Journal of bacteriology 178, 3939–3948.
416 Pyatibratov, M.G., Beznosov, S.N., Rachel, R., Tiktopulo, E.I., Surin, A.K., Syutkin, A.S.,
417 Fedorov, O.V., 2008. Alternative flagellar filament types in the haloarchaeon Haloarcula
418 marismortui. Canadian Journal of Microbiology 54, 835–844.
419 Quintero, E.J., Busch, K., Weiner, R.M., 1998. Spatial and Temporal Deposition of Adhesive
420 Extracellular Polysaccharide Capsule and Fimbriae by Hyphomonas Strain MHS-3. Applied
421 and Environmental Microbiology 64, 1246–1255.
422 Schopf, J.W., Kudryavtsev, A.B., Agresti, D.G., Wdowiak, T.J., Czaja, A.D., 2002. Laser–
423 Raman imagery of Earth's earliest fossils. Nature 416, 73–76.

Siano, R., Kooistra, W.H.C.F., Montresor, M., Zingone, A., 2009. Unarmoured and thin-walled dinoflagellates from the Gulf of Naples, with the description of Woloszynskia cincta sp. nov. (Dinophyceae, Suessiales). Phycologia 48, 44–65.

Southam, G., Kalmokoff, M.L., Jarrell, K.F., Koval, S.F., Beveridge, T.J., 1990. Isolation, characterization, and cellular insertion of the flagella from two strains of the archaebacterium Methanospirillum hungatei. Journal of Bacteriology 172, 3221–3228.

Sugimoto, S., Okuda, K., Miyakawa, R., Sato, M., Arita-Morioka, K., Chiba, A., Yamanaka, K., Ogura, T., Mizunoe, Y., Sato, C., 2016. Imaging of bacterial multicellular behaviour in biofilms in liquid by atmospheric scanning electron microscopy. Scientific Reports 6, 25889.

Sugitani, K., Lepot, K., Nagaoka, T., Mimura, K., Van Kranendonk, M., Oehler, D.Z., Walter, M.R., 2010. Biogenicity of Morphologically Diverse Carbonaceous Microstructures from the ca. 3400 Ma Strelley Pool Formation, in the Pilbara Craton, Western Australia. Astrobiology 10, 899–920.

Sugitani, K., Mimura, K., Nagaoka, T., Lepot, K., Takeuchi, M., 2013. Microfossil assemblage from the 3400Ma Strelley Pool Formation in the Pilbara Craton, Western Australia: Results form a new locality. Precambrian Research 226, 59–74.

Sugitani, K., Mimura, K., Takeuchi, M., Lepot, K., Ito, S., Javaux, E.J., 2015. Early evolution of large micro-organisms with cytological complexity revealed by microanalyses of 3.4 Ga organic-walled microfossils. Geobiology 13, 507–521.

Vasilyeva, L.V., Omelchenko, M.V., Berestovskaya, Y.Y., Lysenko, A.M., Abraham, W.-R., Dedysh, S.N., Zavarzin, G.A., 2006. Asticcacaulis benevestitus sp. nov., a psychrotolerant, dimorphic, prosthecate bacterium from tundra wetland soil. International Journal of Systematic and Evolutionary Microbiology 56, 2083–2088.

447 Wacey, D., Kilburn, M.R., Saunders, M., Cliff, J., Brasier, M.D., 2011. Microfossils of sulphur-
448 metabolizing cells in 3.4-billion-year-old rocks of Western Australia. Nature Geoscience 4,
449 698–702.
450 Wacey, D., Saunders, M., Kong, C., Brasier, A., Brasier, M., 2016. 3.46 Ga Apex chert
451 'microfossils' reinterpreted as mineral artefacts produced during phyllosilicate exfoliation.
452 Gondwana Research 36, 296–313.
453 Wagner, J.K., Setayeshgar, S., Sharon, L.A., Reilly, J.P., Brun, Y.V., 2006. A nutrient uptake
454 role for bacterial cell envelope extensions. Proceedings of the National Academy of Sciences
455 103, 11772–11777.
456 Wang, H., Lu, D., Huang, H., Göbel, J., Dai, X., Xia, P., 2011. First observation of Karlodinium
457 veneficum from the East China Sea and the coastal waters of Germany. Acta Oceanologica
458 Sinica 30, 112–121.
459 Wang, Y., Chen, Y., Lavin, C., Gretz, M.R., 2000. Extracellular matrix assembly in diatoms
460 (Bacillariophyceae). iv. ultrastructure of Achnanthes longipes and Cymbella cistula as revealed
461 by high-pressure freezing/freeze substituton and cryo-field emission scanning electron
462 microscopy. Journal of Phycology 36, 367–378.
463 Westall, F., de Ronde, C.E.J., Southam, G., Grassineau, N., Colas, M., Cockell, C., Lammer,
464 H., 2006. Implications of a 3.472–3.333 Gyr-old subaerial microbial mat from the Barberton
465 greenstone belt, South Africa for the UV environmental conditions on the early Earth.
466 Philosophical Transactions of the Royal Society B: Biological Sciences 361, 1857–1876.
467 Wustman, B.A., Gretz, M.R., Hoagland, K.D., 1997. Extracellular Matrix Assembly in Diatoms
468 (Bacillariophyceae) (I. A Model of Adhesives Based on Chemical Characterization and
469 Localization of Polysaccharides from the Marine Diatom Achnanthes longipes and Other
470 Diatoms). Plant Physiology 113, 1059–1069.
471

Chemical degradation of thermally altered silicified organic matter during acid maceration: a case study from the Lower Devonian Rhynie chert

Frédéric Delarue [a*], Thanh Thuy Nguyen Tu [a], Rémi Duhamel [b], Céline Paris [c], François Baudin [d]

[a] *Sorbonne Université, CNRS, EPHE, PSL, UMR 7619 METIS, 4 place Jussieu, F-75005 Paris, France*

[b] *Muséum National d'Histoire Naturelle, Sorbonne Université, UMR 7590, IRD, IMPMC, F-75005 Paris, France*

[c] *Sorbonne Université, CNRS, UMR 8233 MONARIS, 75005, 4 place Jussieu, F-75005 Paris, Paris, France*

[d] *Sorbonne Université, CNRS, UMR 7193 ISTeP, 4 place Jussieu, F-75005 Paris, France*

*Correspondence to: frederic.delarue@sorbonne-universite.fr

ABSTRACT

The effect of standard acid maceration on organic matter (OM) from ancient silicified sediments remains undocumented. Early silicification favours preservation of organic moieties against thermal alteration over time. In this study, we investigated the effects of acid maceration on the structure of OM isolated from the Lower Devonian Rhynie chert. The structure of OM was investigated by combining Rock-Eval pyrolysis and Raman spectroscopy. Besides a loss of thermolabile organic matter owing to solvent extraction, Rock-Eval pyrolysis showed that standard acid maceration also causes a loss of C-H emissions at high pyrolysis temperature (> 500 °C). The standard acid maceration procedure was also associated with the disappearance of the D4 and D5 Raman spectrum shoulders assigned to C–H bonds in aliphatics and bitumens, respectively, entrapped in the macromolecular network. Taken together, Rock-Eval pyrolysis and Raman spectroscopy indicate that standard acid maceration can lead to the chemical degradation of syngenetic hydro-carbonaceous moieties of OM isolated from ancient silicified and thermally altered sediments. In sediments having experienced early silicification, which hampers bitumen migration and favours pyrobitumen formation, we suggest that novel in situ molecular analytical techniques are required to provide a thorough examination of the syngenetic molecular content independent of the soluble/insoluble operational definition.

1. Introduction

The chemical composition of ancient organic matter (OM) attests to turning points in the evolution of life during the history of the Earth (Summons et al., 1988; Edwards et al., 1997; Love et al., 2008; Duda et al., 2016; Nguyen et al., 2019; Love et al., 2020). However, investigating the structural and chemical compositions of ancient OM is still a challenging issue as thermal alteration during geological times results in losses of pristine molecular and

elemental content. Since ancient sediments and metasediments are generally depleted in OM, isolation procedures have typically been employed before applying analytical techniques to investigate the chemical composition of ancient OM, notably at the molecular scale. Historically, in the field of organic geochemistry, isolation of organic-insoluble and mineral-free OM is performed through a standard acid maceration procedure involving maceration followed by successive organic solvent extractions (e.g., dichloromethane [DCM] and methanol [MeOH]) and demineralisation with acid (e.g., hydrochloric [HCl] and hydrofluoric [HF]). This physical and chemical maceration procedure (HMM) yields kerogen, which is defined as insoluble macromolecular OM (Durand, 1980; Vandenbroucke and Largeau, 2007). Several investigations have suggested that acid maceration does not significantly modify the structure of kerogens from ancient rocks (Larsen et al., 1989; Vandenbroucke and Largeau, 2007; Aboulkas and El Harfi, 2009). However, there is contrasting evidence that acid maceration of coals can lead to either a rise in carbon structural order (Zhang et al., 2016) or a decrease in hydrocarbon content (Tekely et al., 1987). Moreover, Kebukawa et al. (2019) demonstrated the contrasting effects of acid maceration by comparing the chemical structure of bulk chondrites to their corresponding insoluble OM fractions. Insoluble OM from type 3 chondrite was depleted in aliphatic moieties in comparison to the bulk type 3 chondrite starting material. However, the effect of acid maceration varied among the different chondrite groups studied (Kebukawa et al., 2019). Thus, according to current literature, it therefore seems that the chemical stability of thermally altered OM to standard acid maceration cannot simply be assumed.

Among ancient sedimentary rocks, silicified sediments are of interest as they are essential geological archives of biological evolution throughout Earth's history. However, there is often very little OM remaining in these sediments and acid maceration procedures are required to concentrate it before studying its molecular content. Occurring prior to cell lysis

and early degradation of organic matter, rapid silicification leads to a closed chemical system by reducing sediment porosity (Boyce et al., 2002; Ledevin et al., 2014), which favours preservation of organic remnants against thermal alteration (Alleon et al., 2016). Using geochemical micrometre-scale analysis tools, it was demonstrated that some silicified Precambrian organic-walled microfossils are composed of significant amounts of carbonyl, phenolic, carboxylic, hydroxyl, and amide functional groups, despite being subjected to peak temperatures of up to 300 °C (Alleon et al., 2016). However, standard acid maceration procedures applied to ancient silicified sediments have the potential to degrade syngenetic OM through solvent extraction and acid hydrolysis of bitumens and chemically labile organic moieties, respectively. Such degradation, if it occurs, implies that a substantial amount of the initial molecular content depicting the evolution of life, past environmental conditions, and/or thermal maturation may be lost in the process. Further investigations on the effect of standard acid maceration on the chemical structure of ancient thermally altered silicified OM are therefore required.

Our aim in this study was to investigate the effect of the standard acid maceration procedure on the chemical structure of ancient silicified OM. We selected the iconic Lower Devonian Rhynie chert, the earliest preserved terrestrial ecosystem owing to a rapid and complete silicification through siliceous hot-spring deposits (Trewin, 2003; Preston and Genge, 2010). Despite the exceptional preservation of fossil plants, fungi, insects, and other organisms, the overall organic carbon content of Rhynie chert is very low (Summons et al., 1996). It therefore typically requires acid maceration to access the molecular signature(s). The Rhynie chert therefore constitutes a case study to evaluate the impact of standard acid maceration on the chemical structure of ancient thermally altered silicified OM. To this end, OM was isolated according to two acid maceration procedures: (1) a high-manipulation maceration (HMM), which followed the standard treatments generally applied to geological

92 samples, and (2) a low-manipulation maceration (LMM), which minimized chemical
93 degradation by avoiding organic solvents and HCl. Rock-Eval pyrolysis and Raman
94 spectroscopy were used to assess the chemical structure of the OM isolated by each
95 procedure. Comparison of the so-obtained chemical structures allowed us to estimate the
96 minimum amount of chemical degradation imparted by HMM maceration.
97
98 **2. Material and methods**
99 *2.1. The Rhynie chert*
100 Situated in Aberdeenshire (Scotland), the Rhynie chert is a Konservat-Lagerstätte. It is
101 hosted by the Dryden Flags Formation, which is characterised by a succession of Lower
102 Devonian sedimentary and volcanic rocks (Rice et al., 2002). Pragian–earliest Emsian in age
103 (407.1 ± 2.2 Ma; Mark et al., 2011), the Rhynie chert is composed primarily of
104 microcrystalline silica and was deposited as siliceous sinter from subaerial hot springs
105 systems (Rice et al., 1995).
106
107 *2.2. High- and low-manipulation maceration procedures*
108 HMM and LMM procedures were performed on similar portions of the same rock
109 sample. HMM was performed on ~30 g of crushed rock. Solvent extraction was first
110 performed on rock powder using a mixture of DCM and MeOH (2:1; v:v). Carbonates were
111 then removed at room temperature using HCl (37%; reagent grade) to minimise the formation
112 of fluorides during subsequent HF/HCl maceration. Samples were then centrifuged and
113 washed with ultrapure water until reaching neutrality. Concentration of OM was achieved
114 through acid maceration at room temperature in a mixture of HF (40%, reagent grade) and
115 HCl (2:1, v/v; reagent grade). Samples were centrifuged and washed with ultrapure water to
116 reach neutrality. Finally, HCl (37%; reagent grade) at 60 °C (24 h) was used to degrade

117 neoformed fluorides. After an additional step of solvent extraction using a mixture of DCM
118 and MeOH (2:1, v/v), the isolated OM was again centrifuged/washed with ultrapure water
119 until reaching neutrality. Samples were then air-dried at 60 °C after final rinsing in acetone.
120 Hereafter, OM isolated by the HMM procedure is referred to as OHMM.
121 LMM was performed by first fragmenting ~30 g of rock samples into ~3 g rock chips.
122 Rock chips were cleaned using ultrapure water and a mixture of DCM and MeOH (2:1, v/v)
123 and were then placed directly in a Teflon vessel filled with HF (40%, reagent grade) at room
124 temperature. After 48 h, successive centrifugation and rinsing steps using ultrapure water
125 were performed until reaching neutrality. Samples were then air-dried at 60 °C. Hereafter,
126 OM isolated by the LMM procedure is referred to as OLMM.
127
128 *2.3. Rock-Eval pyrolysis*
129 OHMM and OLMM were analysed using Rock-Eval 6 (Vinci Technologies) following
130 the standard pyrolysis protocol described in Behar et al. (2001). Performed in a N_2
131 atmosphere, Rock-Eval pyrolysis comprises two steps: an isothermal phase held for 3 minutes
132 followed by a rise in pyrolysis temperature from 300 to 650 °C at a rate of 25 °C/min. After
133 pyrolysis, the residual material was then heated from 300 °C to 850 °C under purified air in an
134 oxidation oven in order to calculate total organic carbon (TOC) value (see Behar et al., 2001
135 for further details about calculation procedure). Released hydrocarbons (HC) were
136 continuously quantified by a flame ionisation detector (S1 and S2, for the first and second
137 pyrolysis steps, respectively, in mg HC/g of sample) while released CO and CO_2 were
138 continuously and simultaneously monitored by infrared detectors during both pyrolysis
139 (S3CO and S3CO_2) and combustion (S4CO and S4CO_2). Quantification of the amount of
140 effluents led to the determination of the TOC (wt%), of the Hydrogen Index (HI, defined as
141 S2×100/TOC, in mg HC/g of TOC) and of the Oxygen Index (OI; defined as S3×100/TOC, in

142 mg CO_2/g of TOC). The pyrolysis temperature associated with the maximum release of
143 hydrocarbons, called "TpkS2", was also determined.
144
145 *2.4. Raman spectroscopy*
146 Raman spectroscopy analysis was performed using a Renishaw inVia micro-
147 spectrometer equipped with a 532 nm argon laser. The spectrometer was first calibrated using
148 a silicon standard before each session. For each sample analysis, the laser was focused using a
149 Leica microscope with a ×50 objective and the spectra were recorded in the 1000–1900 cm^{-1}
150 first order spectral window including the defect (D) and graphite (G) peaks (Fig. 1). The laser
151 power at the sample surface was kept below 1 mW to prevent thermal alteration of isolated
152 OM (Everall et al., 1991). Spectra acquisition was achieved after two iterations using a time
153 exposure of 40 s. After linear correction of the baseline between 1000 and 1900 cm^{-1} and
154 spectra normalization, we identified Raman peaks according to the nomenclature defined in
155 Romero-Sarmiento et al. (2014).
156 The heights of the sub-bands D1 (~1365 cm^{-1}), D4 (~1285 cm^{-1}), D5 (~1445 cm^{-1}) and
157 G+D2 (~1600 cm^{-1}; Fig. 1) were then determined to compute the I_{D1}/I_{G+D2}, I_{D4}/I_{G+D2} and
158 I_{D5}/I_{G+D2}, ratios. Slopes α_{D4} (determined between 1265 and 1300 cm^{-1} Raman shift) and α_{D5}
159 (determined between 1415 and 1445 cm^{-1} Raman shift) were determined to geometrically
160 evaluate the expression of D4 and D5 shoulders on the D band.
161
162 **3. Results and discussion**
163 The TOC of OHMM and OLMM samples was measured to determine the efficiency
164 of rock mineralization through HMM and LMM, respectively. The TOC in all OHMM and
165 OLMM samples was low (25.4% and 27.5% respectively; Table 1) suggesting that the
166 preservation and/or neoformation of substantial mineral content had occurred during both

167 procedures. The OI was approximately 15 mg and 59 mg CO_2/g TOC in OHMM and OLMM,
168 respectively (Table 1). The higher OI in OLMM is partially explained by the higher level of
169 CO_2 emissions during the first isothermal step, showing that they are mostly related to
170 desorbable OM (Fig. 2). Such a result is in line with previous investigations on coals
171 suggesting that acid maceration can lead to a rise in oxygen content resulting possibly from
172 the neoformation of carboxylic groups replacing carboxylate through ion exchange (Larsen et
173 al., 1989). Higher levels of CO_2 emissions were also recorded for OLMM during the rise in
174 pyrolysis temperature from 300 to 650 °C (Fig. 2). In this pyrolysis temperature range, CO_2
175 emissions appeared to be independent of hydrocarbon emissions suggesting that they do not
176 correspond to the thermal cracking of the macromolecular network.
177 OHMM and OLMM isolated from the Rhynie chert were characterised by a TpkS2 of
178 481 °C and 504 °C, respectively (Table 1). In every type of kerogen, these pyrolysis
179 temperatures are commonly assigned to OM that has been subjected to high thermal
180 alteration. Consistent with high TpkS2 values, pyrolysis of OHMM and of OLMM released
181 low amounts of HC as evidenced by HI of 46 HC/g TOC and 68 mg HC/g TOC, respectively.
182 Together, high TpkS2 and low HI imply that OM from the Rhynie chert falls at the transition
183 between the oil and gas windows registered by TpkS2 ranging between 470 °C and 505 °C in
184 analogous Type III kerogens (Espitalié et al., 1986). Hydrocarbon release during Rock-Eval
185 pyrolysis was higher in OLMM than in OHMM (Table 1). The S1 value for OLMM was
186 about 320% higher than for OHMM (Table 1), which suggests that thermolabile OM was
187 more abundant in OLMM than in OHMM. This is consistent with the fact that OLMM was
188 not subjected to organic solvent extractions, which have been shown to dramatically reduce
189 S1 values (Delvaux et al., 1990). Between 300 and 350 °C, no release of hydrocarbons was
190 observed suggesting a virtual absence of residual heavy oil and/or of pyrobitumen in both
191 OHMM and OLMM (Fig. 2; Clementz, 1979; Sanei et al., 2015). The S2 curves for OHMM

192 and OLMM differ at high pyrolysis temperature (> 500 °C), at which point a broad shoulder
193 is only observed in OLMM (Fig. 2). The occurrence of this thermorecalcitrant OM in OLMM
194 mostly explains its higher HI, in the absence of solvent extractions and/or hydrochloric acid
195 hydrolysis (Table 1). In turn, this suggests that standard acid maceration can lead to a
196 modification of the macromolecular chemical structure in this ancient silicified OM by
197 promoting a loss of hydrocarbonaceous moieties.

198 Determined on 15 random targets in both OHMM and OLMM, Raman spectra
199 exhibited two broad D and G+D2 bands at around 1365 cm^{-1} and 1600 cm^{-1} in each
200 preparation (Fig. 1). The D band presents a complex structure resulting from the presence of
201 several sub-bands including here, the D4, D1, and D5 bands. In addition to the contribution of
202 amorphous carbon, the D band is dominated by the D1 sub-band corresponding to the
203 breathing mode of the sp^2 aromatic ring within polyaromatic clusters and is attributed to
204 defects in these aromatic structures (Ferrari and Robertson, 2000). The D2 band corresponds
205 to defects in aromatic structure but in contrast to the D1 band, does not include amorphous
206 carbon. A distinct D2 peak (usually centered at about 1620 cm^{-1}) is mainly observed in highly
207 mature OM (Kouketsu et al. 2014) and is not observed in OM studied here. Therefore, the
208 G+D2 band is mostly related to the G band corresponding to in-plane C-C bond stretching in
209 polyaromatic layers from thermally altered materials (Marshall and Marshall, 2014). As the
210 height of the D1 band increases with temperature, the I_{D1}/I_{G+D2} ratio is often used to probe the
211 structural order of OM in the course of carbonization (Table 2; Wopenka and Pasteris, 1993;
212 Quirico et al., 2005; Kouketsu et al., 2014; Delarue et al., 2016). In this study, OHMM and
213 OLMM are characterized by I_{D1}/I_{G+D2} ratios of 0.58 ± 0.02 and 0.52 ± 0.02, respectively
214 (Table 2). This result would imply a higher carbon structural order in OHMM compared to
215 OLMM, which is in agreement with previous findings indicating that standard acid
216 maceration can yield a rise in carbon structural order (Zhang et al., 2016).

The D band also exhibits two shoulders corresponding to the D4 (1285 cm^{-1}) and D5 (1445 cm^{-1}) bands (Fig. 1). The D4 peak is generally assigned to C–H bonds in aliphatics as C-H in aromatics does not seem to directly contribute to the D4 region (Ferralis et al., 2016). The D5 band indicates the presence of hydrocarbons trapped within the organic porosity and has been detected in a few oil and gas shale samples (Romero-Sarmiento et al., 2014; Rouzaud et al., 2015). In the current study, α_{D4} and α_{D5} slopes in Raman spectra were lower in OLMM than in OHMM, consistent with the more pronounced D4 and D5 shoulders in the Raman line of OLMM (Fig. 1; Table 2). However, the more pronounced D4 and D5 shoulders in OLMM were not associated with higher I_{D4}/I_{G+D2} and I_{D5}/I_{G+D2} ratios (Table 2). This could be explained by the higher carbon structural order in OHMM implying a bias in the determination of I_{D4}/I_{G+D2} and I_{D5}/I_{G+D2} ratios. The occurrence of more pronounced D4 and D5 shoulders in OLMM indicate that OLMM is indeed enriched in hydrocarbonaceous moieties, due to the C-H bonds in aliphatics and other entrapped hydrocarbons, relative to OHMM. The presence of entrapped hydrocarbons in the macromolecular network of OLMM likely explains the broad shoulder cracking at high temperature (> 500 °C) as revealed by Rock-Eval pyrolysis (Fig. 2). Both Raman spectroscopy and Rock-Eval pyrolysis suggest that standard acid maceration results in a loss of hydrocarbons in OM isolated from the Rhynie chert. As LMM does not involve the organic solvent extraction used in HMM, part of this hydrocarbon loss is likely due to solvent-extractible OM, which is reflected by the respective S1 values. In contrast to OHMM, OLMM did not involve extraction with HCl, which when mixed with HF has been demonstrated to favour hydrolysis leading to a loss of aliphatic CH and/or CH_2 functional groups in coal (Tekely et al., 1987). Even though our experimental design did not allow us to test the singular effect of HCl hydrolysis, such an effect can be hypothesized to partly explain the loss in aliphatic moieties with HMM treatment.

241 Although the Raman spectroscopy results support the notion that hydrocarbons are lost
242 during HMM, it does not directly allow the extent of this loss to be determined. Following the
243 relationship between H/C and HI (Espitalié et al., 1977), we determined that H/C atomic
244 ratios were 0.53 and 0.57 in OHMM and OLMM, respectively (Table 1). Standard acid
245 maceration therefore led to a reduction of at least about 7–8% of the hydrocarbon content of
246 Rhynie OM. We use "at least" because chemical degradation of hydrocarbons occurring
247 during the isolation of OLMM cannot be straightforwardly excluded. To evaluate this point,
248 Raman spectra were also acquired on in situ OM from thin sections of Rhynie chert
249 (Supplementary information). These in situ Raman spectra were acquired with another Raman
250 spectroscope and on polished thin sections, which can modify the apparent carbon structural
251 order by yielding an increase in the D band (Ammar et al., 2011; Maslova et al., 2012). These
252 issues therefore prevent a straightforward comparison between Raman-derived ratios from in
253 situ OM and from OLMM/OHMM. Nonetheless, the α_{D4} and α_{D5} parameters are independent
254 of the height of the D band and can be used to track a potential effect of LMM procedure. In
255 situ OM presents a mean α_{D4} and α_{D5} of about 31 ± 4 and -24 ± 23, respectively (n = 10),
256 indicating more pronounced D4 and D5 shoulders in the in situ OM compared to OLMM
257 (Supplementary information). This suggests that simple treatment with HF and water also led
258 to a slight loss in aliphatic content. In addition to these hydrocarbon losses related to acid
259 maceration procedures, the estimated 7–8% loss in hydrocarbons can also be considered as
260 minimum estimation because of thermolabile hydrocarbons (S1 parameter), which are not
261 taken into account in the calculation of HI and were more abundant in OLMM than in
262 OHMM.
263 Thermolabile hydrocarbons are tightly linked to soluble OM (Delvaux et al., 1990).
264 However, this soluble OM in ancient sediments is often ignored because its syngeneity can be
265 difficult to prove due to the potential for post-deposit contamination (Brocks et al., 2003a,

2003b; Derenne et al., 2008). However, silicified sediments can be seen as unconventional dual source/reservoir rocks. Indeed, rapid silicification drastically reduces porosity leading to a closed chemical system (Boyce et al., 2002; Ledevin et al., 2014). In such source/reservoir rocks, migration of bitumens was very restricted implying that bitumens and/or pyrobitumens coexisted in close proximity with residual kerogens (Vandenbroucke and Largeau, 2007). Hence, in ancient silicified sediments, bitumens and pyrobitumens can be considered syngenetic.

In contrast to soluble OM, insoluble OM is often considered less prone to late contamination (Derenne et al., 2008). Involving no chemical treatment or low-manipulation procedures, numerous studies have investigated the molecular structure of OM – at the scale of plant fossils – to assess the effects of fossilization or to depict plant evolution and affinities (Ewbank et al., 1996; Edwards et al., 1997; Abbott et al., 1998; Czaja et al., 2009; Quijada et al., 2016). Because a large proportion of the hydrocarbon content of these samples is preserved, these investigations minimized secondary hydrothermal and endolithic contaminations – which can also yield insoluble OM – by studying insoluble OM directly from plant fossils. To avoid contamination and to optimize the study of syngenetic hydrocarbons that can be degraded in the course of acid maceration, the development of in situ molecular micrometre-scale analyses techniques (e.g., time-of-flight secondary ion mass spectrometry and laser micropyrolysis) are of interest. Such techniques have the potential to directly probe the molecular structure of organic fossils independent of the soluble/insoluble operational definition. In addition to insightfully assessing chemical heterogeneity within macrofossils (Boyce et al., 2002; Abbott et al., 2018), in situ molecular micrometre-scale analyses also offers the possibility to study the molecular composition of micrometric to sub-micrometric diffuse particulate OM (Stout, 1993; Greenwood et al., 2001; Yoshioka and

290 Takeda, 2004; Silva et al., 2016). This includes remnants of microorganisms, such as organic-
291 walled microfossils, which are essential organic components of the early geological record.
292 In the specific context of silicified rocks – where silicification prevented migration of
293 bitumens and favoured formation of pyrobitumen in the close vicinity of the residual kerogen
294 – the use of in situ molecular micrometre-scale analyses offers promise in the investigation of
295 the molecular composition of early life found within Archean silicified sediments. Indeed, the
296 emergence of micrometre-scale *in situ* analyses have provided compelling evidence
297 supporting an unexpected and wide chemical heterogeneity among Archean putative organic-
298 walled microfossils (Delarue et al., 2017, 2020; Hickman-Lewis et al., 2020). Overlooked by
299 bulk extraction approaches, this chemical heterogeneity defines a chemically-well preserved
300 end product among the earliest traces of life. Therefore, the precise study of such geological
301 archives requires further development of in situ molecular micrometre-scale analyses Such
302 techniques may pave the way to document biological and abiotic processes and affinities of
303 the earliest putative remnants of life by: (i) focussing on chemically well preserved
304 specimens, (ii) without the use of chemical extraction and maceration techniques, which can
305 degrade aliphatic moieties preserved in sediments subjected to early and prompt silicification.
306

307 **4. Conclusions**

308 In this study, we investigated the impact of standard acid maceration on the chemical
309 structure of silicified OM from the Lower Devonian Rhynie chert. Using Rock-Eval pyrolysis
310 and Raman spectroscopy, we assessed the chemical structure of OM isolated by two different
311 physical and chemical manipulation procedures. Results from Rock-Eval pyrolysis and
312 Raman spectroscopy converged to demonstrate that the standard procedure of OM isolation
313 led to a significant and substantial degradation of hydrocarbons. These chemical alterations
314 indicate that a significant amount of molecular content is lost as a result of standard acid

315 maceration procedures, thus preventing a thorough examination of the molecular content of
316 organic remnants in thermally altered silicified sediments.
317
318 **Acknowledgements**
319 Authors are grateful to Andrew Ross (Department of Natural Sciences, National
320 Museum of Scotland, Edinburgh) for providing the Rhynie chert sample. We also thank F.
321 Savignac (ISTeP) for Rock-Eval pyrolysis and O. Belhadj (CRCC) for Raman spectroscopy.
322 We also acknowledge K. Liitschwager for proofreading the English writing of this
323 manuscript. J.K. Volkman, G.D. Abbott, anonymous reviewers and C.K. Boyce are
324 acknowledged for their constructive comments on the former versions of the manuscript.
325
326 **References**
327 Abbott, G.D., Ewbank, G., Edwards, D., Wang, G.-Y., 1998. Molecular characterization of
328 some enigmatic Lower Devonian fossils. Geochimica et Cosmochimica Acta 62,
329 1407–1418.
330 Abbott, G.D., Fletcher, I.W., Tardio, S., Hack, E., 2018. Exploring the geochemical
331 distribution of organic carbon in early land plants: a novel approach. Philosophical
332 Transactions of the Royal Society B: Biological Sciences 373, 20160499.
333 Aboulkas, A., El Harfi, K., 2009. Effects of acid treatments on Moroccan Tarfaya oil shale
334 and pyrolysis of oil shale and their kerogen. Journal of Fuel Chemistry and
335 Technology 37, 659–667.
336 Alleon, J., Bernard, S., Le Guillou, C., Daval, D., Skouri-Panet, F., Pont, S., Delbes, L.,
337 Robert, F., 2016. Early entombment within silica minimizes the molecular degradation
338 of microorganisms during advanced diagenesis. Chemical Geology 437, 98–108.
339 Ammar, M.R., Charon, E., Rouzaud, J.-N., Aleon, J., Guimbretière, G., Simon, P., 2011. On a

reliable structural characterization of polished carbons in meteorites by Raman microspectroscopy. Spectroscopy Letters 44, 535–538.

Behar, F., Beaumont, V., De B. Penteado, H.L., 2001. Rock-Eval 6 Technology: Performances and Developments. Oil & Gas Science and Technology 56, 111–134.

Boyce, C.K., Cody, G.D., Feser, M., Jacobsen, C., Knoll, A.H., Wirick, S., 2002. Organic chemical differentiation within fossil plant cell walls detected with X-ray spectromicroscopy. Geology 30, 1039-1042.

Brocks, J.J., Buick, R., Logan, G.A., Summons, R.E., 2003a. Composition and syngeneity of molecular fossils from the 2.78 to 2.45 billion-year-old Mount Bruce Supergroup, Pilbara Craton, Western Australia. Geochimica et Cosmochimica Acta 67, 4289–4319.

Brocks, J.J., Love, G.D., Snape, C.E., Logan, G.A., Summons, R.E., Buick, R., 2003b. Release of bound aromatic hydrocarbons from late Archean and Mesoproterozoic kerogens via hydropyrolysis. Geochimica et Cosmochimica Acta 67, 1521–1530.

Czaja, A.D., Kudryavtsev, A.B., Cody, G.D., Schopf, J.W., 2009. Characterization of permineralized kerogen from an Eocene fossil fern. Organic Geochemistry 40, 353–364.

Clementz, D., 1979. Effect of oil and bitumen saturation on source-rock pyrolysis: Geologic notes. AAPG Bulletin 63. doi:10.1306/2F918919-16CE-11D7-8645000102C1865D

Delarue, F., Robert, F., Derenne, S., Tartèse, R., Jauvion, C., Bernard, S., Pont, S., Gonzalez-Cano, A., Duhamel, R., Sugitani, K., 2020. Out of rock: A new look at the morphological and geochemical preservation of microfossils from the 3.46 Gyr-old Strelley Pool Formation. Precambrian Research 336, 105472.

Delarue, F., Robert, F., Sugitani, K., Tartèse, R., Duhamel, R., Derenne, S., 2017. Investigation of the geochemical preservation of ca. 3.0 Ga permineralized and encapsulated microfossils by nanoscale secondary ion mass spectrometry.

365 Astrobiology 17, 1192–1202.
366 Delarue, F., Rouzaud, J.-N., Derenne, S., Bourbin, M., Westall, F., Kremer, B., Sugitani, K.,
367 Deldicque, D., Robert, F., 2016. The Raman-derived carbonization continuum: A tool
368 to select the best preserved molecular structures in Archean kerogens. Astrobiology
369 16, 407–417.
370 Delvaux, D., Martin, H., Leplat, P., Paulet, J., 1990. Comparative Rock-Eval pyrolysis as an
371 improved tool for sedimentary organic matter analysis. Organic Geochemistry 16,
372 1221–1229.
373 Derenne, S., Robert, F., Skrzypczak-Bonduelle, A., Gourier, D., Binet, L., Rouzaud, J.-N.,
374 2008. Molecular evidence for life in the 3.5 billion year old Warrawoona chert. Earth
375 and Planetary Science Letters 272, 476–480.
376 Duda, J.-P., Thiel, V., Reitner, J., Grazhdankin, D., 2016. Opening up a window into
377 ecosystems with Ediacara-type organisms: preservation of molecular fossils in the
378 Khatyspyt Lagerstätte (Arctic Siberia). PalZ 90, 659–671.
379 Durand, B. (Ed.), 1980. Kerogen, Insoluble Organic Matter from Sedimentary Rocks.
380 Editions Technip 27, Paris, pp. 519.
381 Edwards, D., Ewbank, G., Abbott, G.D., 1997. Flash pyrolysis of the outer cortical tissues in
382 Lower Devonian *Psilophyton dawsonii*. Botanical Journal of the Linnean Society 124,
383 345–360.
384 Espitalié, J., 1986. Use of Tmax as a maturation index for different types of organic matter:
385 comparison with vitrinite reflectance. Collection colloques et séminaires - Institut
386 français du pétrole pp. 475–496.
387 Espitalié, J., Laporte, J.L., Madec, M., Marquis, F., Leplat, P., Paulet, J., Boutefeu, A., 1977.
388 Méthode rapide de caractérisation des roches mètres, de leur potentiel pétrolier et de
389 leur degré d'évolution. Revue de l'Institut Français du Pétrole 32, 23–42.

390 Everall, N.J., Lumsdon, J., Christopher, D.J., 1991. The effect of laser-induced heating upon
391 the vibrational Raman spectra of graphites and carbon fibres. Carbon 29, 133–137.
392 Ewbank, G., Edwards, D., Abbott, G.D., 1996. Chemical characterization of Lower Devonian
393 vascular plants. Organic Geochemistry 25, 461–473.
394 Ferralis, N., Matys, E.D., Knoll, A.H., Hallmann, C., Summons, R.E., 2016. Rapid, direct and
395 non-destructive assessment of fossil organic matter via microRaman spectroscopy.
396 Carbon 108, 440–449.
397 Ferrari, A.C., Robertson, J., 2000. Interpretation of Raman spectra of disordered and
398 amorphous carbon. Physical Review B 61, 14095–14107.
399 Greenwood, P.F., George, S.C., Pickel, W., Zhu, Y., Zhong, N., 2001. In situ analytical
400 pyrolysis of coal macerals and solid bitumens by laser micropyrolysis GC–MS.
401 Journal of Analytical and Applied Pyrolysis 58–59, 237–253.
402 Hickman-Lewis, K., Westall, F., Cavalazzi, B., 2020. Diverse communities of Bacteria and
403 Archaea flourished in Palaeoarchaean (3.5–3.3 Ga) microbial mats. Palaeontology 63,
404 1007–1033.
405 Kebukawa, Y., Alexander, C.M.O., Cody, G.D., 2019. Comparison of FT-IR spectra of bulk
406 and acid insoluble organic matter in chondritic meteorites: An implication for missing
407 carbon during demineralization. Meteoritics & Planetary Science 54, 1632–1641.
408 Kouketsu, Y., Mizukami, T., Mori, H., Endo, S., Aoya, M., Hara, H., Nakamura, D., Wallis,
409 S., 2014. A new approach to develop the Raman carbonaceous material
410 geothermometer for low-grade metamorphism using peak width: Raman CM
411 geothermometer using FWHM. Island Arc 23, 33–50.
412 Larsen, J.W., Pan, C.S., Shawver, S., 1989. Effect of demineralization on the macromolecular
413 structure of coals. Energy & Fuels 3, 557–561.
414 Ledevin, M., Arndt, N., Simionovici, A., Jaillard, E., Ulrich, M., 2014. Silica precipitation

415 triggered by clastic sedimentation in the Archean: New petrographic evidence from
416 cherts of the Kromberg type section, South Africa. Precambrian Research 255, 316–
417 334.
418 Love, G.D., Stalvies, C., Grosjean, E., Meredith, W., Snape, C.E., 2008. Analysis of
419 molecular biomarkers covalently bound within Neoproterozoic sedimentary kerogen.
420 The Paleontological Society Papers 14, 67–83.
421 Love, G.D., Zumberge, J.A., Cárdenas, P., Sperling, E.A., Rohrssen, M., Grosjean, E.,
422 Grotzinger, J.P., Summons, R.E., 2020. Sources of C_{30} steroid biomarkers in
423 Neoproterozoic–Cambrian rocks and oils. Nature Ecology & Evolution 4, 34–36.
424 Mark, D.F., Rice, C.M., Fallick, A.E., Trewin, N.H., Lee, M.R., Boyce, A., Lee, J.K.W.,
425 2011. $^{40}Ar/^{39}Ar$ dating of hydrothermal activity, biota and gold mineralization in the
426 Rhynie hot-spring system, Aberdeenshire, Scotland. Geochimica et Cosmochimica
427 Acta 75, 555–569.
428 Marshall, C.P., Marshall, A.O., 2014. Raman spectroscopy as a screening tool for ancient life
429 detection on Mars. Philosophical Transactions of the Royal Society A: Mathematical,
430 Physical and Engineering Sciences 372, 20140195.
431 Maslova, O.A., Ammar, M.R., Guimbretière, G., Rouzaud, J.-N., Simon, P., 2012.
432 Determination of crystallite size in polished graphitized carbon by Raman
433 spectroscopy. Physical Review B 86, 134205.
434 Nguyen, K., Love, G.D., Zumberge, J.A., Kelly, A.E., Owens, J.D., Rohrssen, M.K., Bates,
435 S.M., Cai, C., Lyons, T.W., 2019. Absence of biomarker evidence for early eukaryotic
436 life from the Mesoproterozoic Roper Group: Searching across a marine redox gradient
437 in mid-Proterozoic habitability. Geobiology 17, 247–260.
438 Preston, L.J., Genge, M.J., 2010. The Rhynie Chert, Scotland, and the search for life on Mars.
439 Astrobiology 10, 549–560.

Quijada, M., Riboulleau, A., Strother, P., Taylor, W., Mezzetti, A., Versteegh, G.J.M., 2016. Protosalvinia revisited, new evidence for a land plant affinity. Review of Palaeobotany and Palynology 227, 52–64.

Quirico, E., Rouzaud, J.-N., Bonal, L., Montagnac, G., 2005. Maturation grade of coals as revealed by Raman spectroscopy: Progress and problems. Spectrochimica Acta Part A: Molecular and Biomolecular Spectroscopy 61, 2368–2377.

Rice, C.M., Ashcroft, W.A., Batten, D.J., Boyce, A.J., Caulfield, J.B.D., Fallick, A.E., Hole, M.J., Jones, E., Pearson, M.J., Rogers, G., Saxton, J.M., Stuart, F.M., Trewin, N.H., Turner, G., 1995. A Devonian auriferous hot spring system, Rhynie, Scotland. Journal of the Geological Society 152, 229–250.

Rice, C.M., Trewin, N.H., Anderson, L.I., 2002. Geological setting of the Early Devonian Rhynie cherts, Aberdeenshire, Scotland: an early terrestrial hot spring system. Journal of the Geological Society 159, 203–214.

Romero-Sarmiento, M.-F., Rouzaud, J.-N., Bernard, S., Deldicque, D., Thomas, M., Littke, R., 2014. Evolution of Barnett Shale organic carbon structure and nanostructure with increasing maturation. Organic Geochemistry 71, 7–16.

Rouzaud, J.-N., Deldicque, D., Charon, É., Pageot, J., 2015. Carbons at the heart of questions on energy and environment: A nanostructural approach. Comptes Rendus Geoscience 347, 124–133.

Sanei, H., Wood, J.M., Ardakani, O.H., Clarkson, C.R., Jiang, C., 2015. Characterization of organic matter fractions in an unconventional tight gas siltstone reservoir. International Journal of Coal Geology 150–151, 296–305.

Silva, T.F. da, Mendonça Filho, J.G., da Silva, M.C., de Oliveira, A.D., de Souza, J.T., Rondon, N.F., 2016. Botryococcus braunii versus *Gloeocapsomorpha prisca* : Chemical composition correlation using laser micropyrolysis-gas

chromatography/mass spectrometer (LmPy-GCMSMS). International Journal of Coal Geology 168, 71–79.

Stout, S.A., 1993. Lasers in organic petrology and organic geochemistry, II. In-situ laser micropyrolysis-GCMS of coal macerals. International Journal of Coal Geology 24, 309–331.

Summons, R.E., Jahnke, L.L., Simoneit, B.R.T., 1996. Lipid biomarkers for bacterial ecosystems: studies of cultured organisms, hydrothermal environments and ancient sediments. In: Evolution of Hydrothermal Ecosystems on Earth (and Mars?). Wiley, Chichester, pp. 174–194.

Summons, R.E., Brassell, S.C., Eglinton, G., Evans, E., Horodyski, R.J., Robinson, N., Ward, D.M., 1988. Distinctive hydrocarbon biomarkers from fossiliferous sediment of the Late Proterozoic Walcott Member, Chuar Group, Grand Canyon, Arizona. Geochimica et Cosmochimica Acta 52, 2625–2637.

Tekely, P., Nicole, D., Delpuech, J. -j., Totino, E., Muller, J.F., 1987. Chemical structure changes in coals after low-temperature oxidation and demineralization by acid treatment as revealed by high resolution solid state ^{13}C NMR. Fuel Processing Technology 15, 225–231.

Trewin, N.H., 2003. History of research on the geology and palaeontology of the Rhynie area, Aberdeenshire, Scotland. Transactions of the Royal Society of Edinburgh: Earth Sciences 94, 285–297.

Vandenbroucke, M., Largeau, C., 2007. Kerogen origin, evolution and structure. Organic Geochemistry 38, 719–833.

Wopenka, B., Pasteris, J.D., 1993. Structural characterization of kerogens to granulite-facies graphite: Applicability of Raman microprobe spectroscopy. American Mineralogist 78, 533–557.

Yoshioka, H., Takeda, N., 2004. Analysis of organic compounds in coal macerals by infrared laser micropyrolysis. Journal of Analytical and Applied Pyrolysis 71, 137–149.

Zhang, L., Li, Z., Yang, Y., Zhou, Y., Kong, B., Li, J., Si, L., 2016. Effect of acid treatment on the characteristics and structures of high-sulfur bituminous coal. Fuel 184, 418–429.

Figure captions

Fig. 1. (a) Typical Raman spectra measured on OHMM (black line) and OLMM (grey line).

Fig. 2. Emissions of (a) hydrocarbons and (b) CO_2 during Rock-Eval pyrolysis of OHMM (black line) and OLMM (grey line). The red curve indicates the pyrolysis temperature program. The green area in (b) indicates the temperature interval, for which CO_2 emissions are included in the calculation of OI.

Table 1: Rock-Eval parameters determined in OHMM and OLMM. *H/C atomic ratio was estimated using the relationship between H/C atomic ratio and HI (H/C = 0.0017 × HI + 0.453) published by Espitalié et al. (1977).

	S1 (mg HC/g)	**S2** (mg HC/g)	**TpkS2** (°C)	**TOC** (%)	**HI** (mg HC/g TOC)	**OI** (mg CO_2/g TOC)	**H/C atomic ratio***
OHMM	0.59	11.76	481	25.4	46	59	0.53
OLMM	2.48	18.83	504	27.5	68	15	0.57

Table 2: Raman-derived parameters (mean value ± S.D.) determined in OHMM and OLMM (n= 15; Wilcoxon rank test).

	I_{D1}/I_{G+D2}	I_{D4}/I_{G+D2}	I_{D5}/I_{G+D2}	α_{D4}	α_{D5}
OHMM	0.58 ± 0.02	0.38 ± 0.02	0.43 ± 0.04	359 ± 35	-288 ± 39
OLMM	0.52 ± 0.02	0.36 ± 0.02	0.31 ± 0.01	202 ± 37	-240 ± 28
p-value	< 0.001	< 0.001	< 0.001	< 0.001	< 0.001

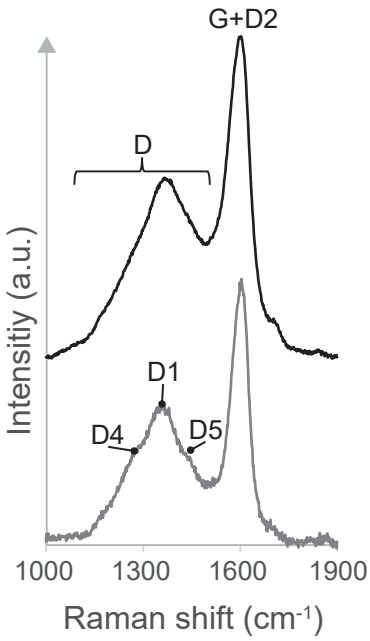
G+D2
D
Intensitiy (a.u.)
D1
D4
D5
1000
1300
1600
1900
Raman shift (cm-1)

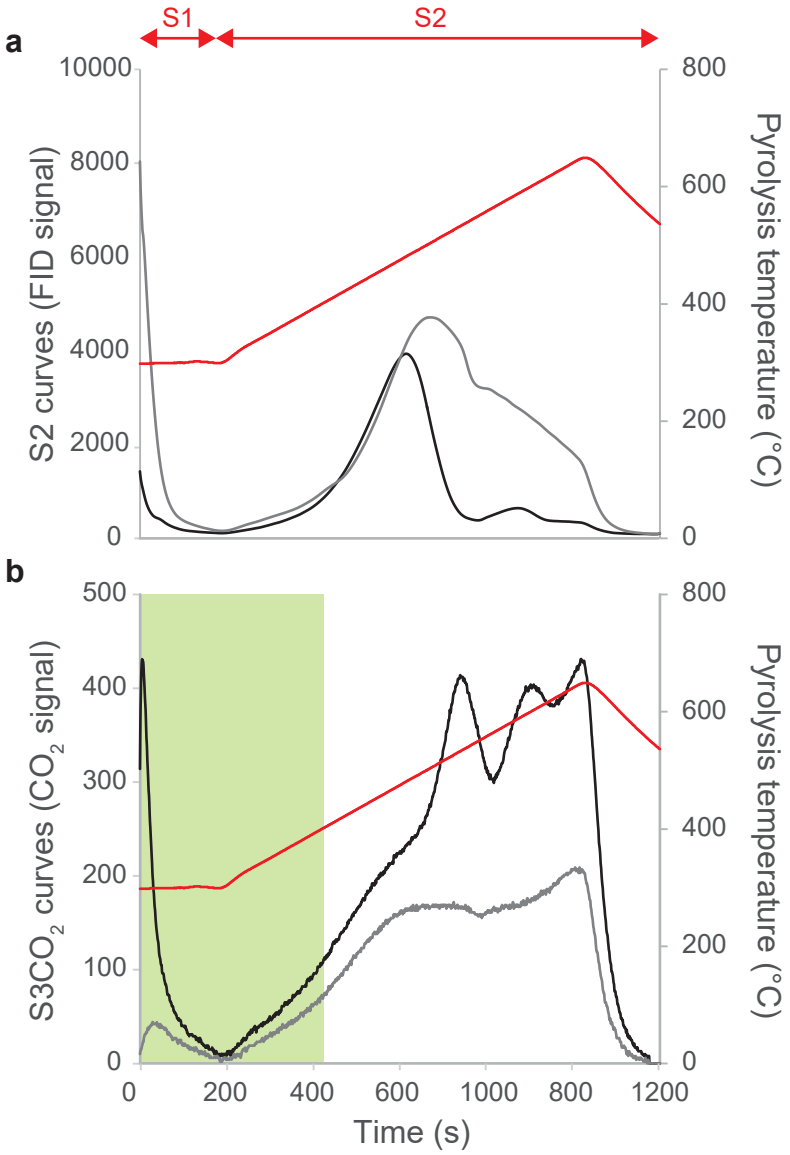
a
S1
S2
10000
8000
6000
4000
2000
0
S2 curves (FID signal)
800
600
400
200
0
Pyrolysis temperature (°C)
b
500
400
300
200
100
0
S3CO2 curves (CO2 signal)
800
600
400
200
0
Pyrolysis temperature (°C)
0
200
400
600
1000
800
1200
Time (s)